On the effect of the tip-clearance ratio on the aeroacoustics of a diffuser-augmented wind turbine

Renewable Energy 152 (2020) 1317–1327

Contents lists available at ScienceDirect

Renewable Energy

journal homepage: www.elsevier.com/locate/renene

On the effect of the tip-clearance ratio on the aeroacoustics of a diffuser-augmented wind turbine

Francesco Avallone*, Daniele Ragni, Damiano Casalino

Department of Aerodynamics, Wind Energy and Propulsion, Delft University of Technology, Kluyverweg 1, 2629HS, Delft, the Netherlands

ARTICLE INFO

Article history:
Received 28 January 2019
Received in revised form
26 December 2019
Accepted 15 January 2020
Available online 23 January 2020

Keywords:
Ducted wind turbine
Urban wind energy
Aeroacoustics

ABSTRACT

Lattice-Boltzmann Very-Large-Eddy Simulations of two Diffuser-Augmented Wind Turbines are carried out to investigate the effect of the tip-clearance (TC) ratio on both the flow field and the far-field noise. The DonQi® wind turbine, a three blades ducted rotor with nominal TC of 2.5%, is chosen as reference test case. The second configuration has TC equal to 0.7%. The latter shows flow separation on the diffuser suction side causing lower velocity at the rotor plane and a reduction of 5% of the thrust coefficient. Flow separation is associated with the break down of the tip vortex immediately after the rotor plane. The TC has an effect on the far-field noise. For angles between 60° and 120°, where 0° corresponds to the axial upstream direction, the blade tonal noise is the dominant source. For other angular directions, noise increase is found for the smaller TC and it associated to an additional noise source located into the gap that can be modeled as a monopole source. It causes an increase of broadband noise at frequencies higher than the third blade passing frequency and tonal peaks at frequencies equal to 4.5 times the blade passing frequency and higher harmonics.

1. Introduction

Wind energy is emerging as a reliable resource for power production. In 2016, it contributed to cover 10.4% of the overall electricity demand in Europe [1] and it is expected to grow up to 29.6% in 2030 [2]. Most of the wind energy production is obtained from wind turbines located close to populated areas for which stringent regulations against visual and acoustic pollution exist.

A possible solution to spread on-shore wind energy is to use small urban wind turbines that can be located close to populated areas, where the presence of buildings disturbs the flow uniformity resulting in lower wind speed with larger turbulent fluctuations. To partially overcome this problem, Diffuser-Augmented Wind Turbines (DAWTs) represent an interesting concept. They are realized by installing a rotor within a diffuser (also named duct or shroud) that increases the wind speed at the rotor location. Recently Shonhiwa and Makaka [3], and Agha et al. [4], reviewed the developments of this technology.

von Betz [5] was the first to propose DAWT as a solution to increase the rated power. Afterwards, many analytical approaches have been developed while few experimental and computational data have been collected. As a matter of fact, in a recent paper, Bontempo and Manna [6] stated that was not possible to validate their semi-analytical model against wind turbine data.

As mentioned earlier, most of the effort has been devoted to the analytical modeling with the goal of estimating the increase in energy production with respect to conventional wind turbines. Before discussing the different findings from several authors, it is worth mentioning that there is lack of consensus on the choice of the reference parameters used to compute the power coefficient. Some authors adopt the rotor disc area while others the duct exit area; the specific definition will be reported in each case. The first analytical model, based on one-dimensional theory, was proposed by de Vries [7] who found that the maximum achievable power coefficient is 0.7698. Afterwards, Hansen et al. [8] derived a momentum theory neglecting the wake mixing; they showed that the Betz limit can be exceeded up to 0.94. Both authors used the rotor area as reference area in the estimation of the power coefficient. Similarly, van Bussel [9] showed that power augmentation up to 2.5 can be achieved with respect to the isolated rotor when a large back pressure is obtained, using the duct exit area as reference surface in the estimation of the power coefficient. Additionally, he showed that the optimal rotor thrust coefficient is equal to 8/9. A similar result was also obtained by Jamieson [10] and by Werle and Presz

* Corresponding author.
E-mail address: f.avallone@tudelft.nl (F. Avallone).

https://doi.org/10.1016/j.renene.2020.01.064

[11]. Khamlaj et al. [12] studied the assumptions behind the analytical models of van Bussel, Jamieson and Werle finding that their are valid only for short duct. More recently, de Oliveira et al. [13] studied, using a panel method, the interaction between a body and an actuator disk where a stationary vortex ring was used to model an axisymmetric shroud. No assumption on the shape of the duct was made. They confirmed that embedding an actuator disk within a duct alters the power coefficient and that the actuator loading, at which the optimal power coefficient is reached, depends on the duct geometry (i.e., the generated lift coefficient). Based on these results, Dighe et al. [14] used Reynolds Averaged Numerical Simulation (RANS) to study the influence of the duct geometry parameters on the extracted power. In these simulations, the rotor was replaced by an actuator disk across which a pressure jump was imposed [15]. They found that the airfoil camber plays the most important role and that power increases until separation occurs behind the rotor plane. Since flow separation along the diffuser suction side can reduce the thrust generated by the DAWT, it is important to consider that it can be promoted by the interaction between the blade tip and the turbulent boundary layer as it happens for ducted fan [16].

Most of the Computational Fluid Dynamic (CFD) literature aimed at the optimization of the DAWT using axi-symmetric two-dimensional steady simulations [8,14,17–22]. For example, Fukano and Jang [18], and Abe and Ohya [19] analyzed the effect of the inflow and rotor loading parameters on the aerodynamic performances of a flanged DWT. The available literature misses a full description of the fluid dynamic flow field for a DAWT that can be helpful for improving the modeling. Due to the complex nature of the hydrodynamic interaction between the wake of the rotor and the diffuser surface, it is necessary to include aspects as non-uniform blade loading [6], swirling of the wake and unsteady fluctuations.

Since DAWTs are installed close to urban areas, they are subject to noise regulations and an aeroacoustics study is necessary. In addition to the prediction of the far-field noise intensity and directivity pattern, the effect of the tip-gap size is investigated because of its relevance for ducted systems [16]. As a matter of fact, DAWT are designed with acoustic liners placed along the diffuser suction side that can trigger transition to turbulence and alter the boundary layer thickness at the rotor plane. This can promote the interaction of the turbulent boundary layer with the blade tip and tip vortices, thus increasing the velocity fluctuations within the gap [16] and the generated noise.

Goal of the manuscript is to provide an answer to the two missing points in the literature: the description of the flow and acoustic fields and how they are affected by the tip-gap size. This is achieved by using lattice-Boltzmann Very-Large Eddy Simulation (LB-VLES) for the solution of the flow field and the Ffwocs-Williams and Hawkings acoustic analogy for the far-field noise [23].

2. Computational method

2.1. Flow solver

The LB method is used to compute the flow field because it was shown to be accurate and efficient in presence of complex flow problems [24–26]. The commercial software 3DS Simulia PowerFLOW 5.5a is used. The software solves the discrete LB equation for a finite number of directions. For a detailed description of the method, the reader can refer to Succi [27] and to Shan et al. [28]; while to Chen and Doolen [29] for a review. The LB method determines the macroscopic flow variables starting from the mesoscopic kinetic equation, i.e. the LB equation. The discretization used for this particular application consists of 19 discrete velocities in three dimensions (D3Q19), involving a third-order truncation of the Chapman-Enskog expansion. It was shown that this scheme accurately approximates the Navier-Stokes equations for a perfect gas at low Mach number in isothermal conditions [30]. The distribution of particles is solved by means of the LB equation on a Cartesian mesh, known as a lattice. An explicit time integration and a collision model are used. The LB equation can then be written as:

$$g_i(\mathbf{x}+\mathbf{c}_i\Delta t, t+\Delta t) - g_i(\mathbf{x},t) = C_i(\mathbf{x},t), \tag{1}$$

where g_i is the particle distribution function along the i-th lattice direction. It statistically describes the particle motion at a position x with a discrete velocity $\mathbf{c}_i$ in the i-th direction at time t. $\mathbf{c}_i\Delta t$ and Δt are space and time increments, respectively. $C_i(\mathbf{x},t)$ is the collision term for which the formulation based on a unique Galilean invariant [31] is used. The equilibrium distribution g_i^{eq} of Maxwell-Boltzmann, conventionally used for small Mach number flows, is adopted [30].

A Very Large Eddy Simulation (VLES) model is implemented to take into account the effect of the sub-grid unresolved scales of turbulence. Following Yakhot and Orszag [32], a two-equations $k-\varepsilon$ Renormalization Group is used to compute a turbulent relaxation time that is added to the viscous relaxation time:

$$\tau_{\text{eff}} = \tau + C_\mu \frac{k^2/\varepsilon}{(1+\eta^2)^{1/2}}, \tag{2}$$

where $C_\mu = 0.09$ and η are a combination of the local strain, local vorticity and local helicity parameters. The term η allows to mitigate the sub-grid scale viscosity in the presence of large resolved vortical structures.

In order to reduce the computational cost, a pressure-gradient-extended wall-model (PGE-WM) is used to approximate the no-slip boundary condition on solid walls [33,34]. The model is based on the extension of the generalized law-of-the-wall model [35] to take into account the effect of pressure gradient. The expression of the PGE-WM is:

$$u^+ = \frac{1}{\kappa}\ln\left(\frac{y^+}{A}\right) + B \tag{3}$$

where

$$B = 5.0, \quad \kappa = 0.41, \quad y^+ = \frac{u_\tau y}{\nu}, \tag{4}$$

and where A is a function of the pressure gradient. It captures the physical consequence that the velocity profile slows down and so expands, due to the presence of the pressure gradient, at least at the early stage of the development. The expression of A is:

$$A = 1 + \frac{f\left|\frac{dp}{ds}\right|}{\tau_w}, \quad \hat{\mathbf{u}}_\mathbf{s}\cdot\frac{dp}{ds} > 0 \tag{5}$$

$$A = 1, \quad \text{otherwise}. \tag{6}$$

In the equations, τ_w is the wall shear stress, dp/ds is the streamwise pressure gradient, $\hat{\mathbf{u}}_\mathbf{s}$ is the unit vector of the local slip velocity and f is a length scale equal to the size the unresolved near-wall region. These equations are iteratively solved from the first cell close to the wall in order to specify the boundary conditions of the turbulence model. For this purpose, a slip algorithm [29], obtained as generalization of a bounce-back and specular reflection process, is used.

2.2. Noise computation

The compressible and time-dependent nature of the transient CFD solution together with the low dissipation and dispersion properties of the LB scheme allow extracting the sound pressure field directly in the near-field up to a cut-off frequency corresponding to approximately 15 voxels per acoustic wavelength.

In the far field, noise is computed by using the FWH equation [23]. The formulation 1A, developed by Farassat [36] and extended to a convective wave equation is used in this study [37,38]. The formulation is implemented in the time domain using a source-time dominant algorithm [39]. Integrations are performed on the surface of the model where the unsteady pressure is recorded with the highest frequency rate available on the finest mesh resolution level (referred to as solid formulation). As a consequence, acoustic monopoles and dipoles distributed on the surface of the DAWT are the only source terms of interest [40] and the non-linear contribution related to the turbulent fluctuations in the wake of the DAWT are neglected.

3. Computational set-up

The DonQi® DAWT, shown in Fig. 1, is used in this manuscript as reference. It consists of a diffuser and a three-blade rotor. The diffuser is obtained as axisymmetric revolution of an airfoil cross section. It was designed by the Nederlands Lucht-en Ruimtevaartcentrum (NLR) and the geometry was made available in the context of the DUCT4U project (STW grant number 12728). The diffuser has diameter equal to $D_{in} = 1.74$ m at the inlet, $D_{th} = 1.54$ m at the throat, $D_{out} = 2.0$ m at the exit and a chord equal to $c_{diff} = 1$ m. The radius of the rotor is $R_0 = 0.75$ m, corresponding to a tip-clearance (TC) ratio, defined as the ratio between the tip clearance and the rotor radius, of 2.5%. The rotor has three blades with a NACA 2207 airfoil of chord length varying from 130 mm at the root to 105 mm at the tip. The twist angle ranges from 40.5° at the root to 0.3° at the tip. The chord (c_b) and twist angle (φ) distribution along the blade radius are plotted in Fig. 2. The blades are connected to a hub (upstream) and a nacelle (downstream). The hub is composed of a cylinder, with diameter and length equal to 125 mm and 100 mm, and an upstream aerodynamically shaped geometry. The latter is obtained trough the rotation of a quarter of an ellipsis with minor axis equal to 100 mm and major axis equal to 125 mm. Similarly, the nacelle has the cylinder length equal to 75 mm and the ellipsis major axis equal to 100 mm.

To study the effect of the tip clearance on the aerodynamic and aeroacoustics performance, a second DAWT is investigated. It is obtained from the reference DonQi® DAWT by extending the final part of the blade up to a tip-clearance ratio of 0.7%. The value of the tip clearance is chosen such that the tip of the blade is submerged in the region of velocity increase near the wall, which is equal to 2.1 mm in the current case.

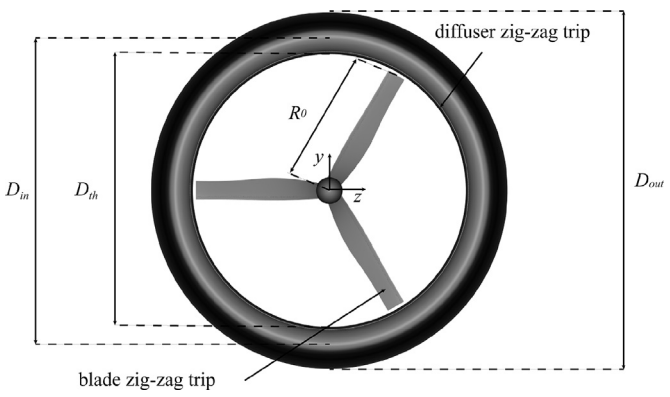

Fig. 1. Front view of the DonQi® wind turbine geometry.

For both configurations, the free-stream velocity is set at $U_\infty = 5$ m/s, which is a characteristic value for urban wind turbines, corresponding to free-stream Mach number and Reynolds number based on the diffuser chord equal to 0.015 and 3.31×10^5. The rotational speed is $\omega = 39.84$ rad/s, corresponding to a tip-speed ratio $\lambda = \omega R_0/U_\infty = 6$, which was found to be the optimal in a previous study on the same wind turbine [41].

Boundary layer transition is forced both on the diffuser and the blades with a zig-zag strip. For the diffuser, an annular zig-zag trip is placed at 10% of the diffuser chord on the suction side (i.e., the inner part of the duct); it has length, height and λ_z (i.e., tip-to-tip distance) respectively equal to 1.5 mm, 2.5 mm and 4 mm. For the blades, the zig-zag trip is applied on both the pressure and suction side; it extends from 15% to 99% of R_0 and it has length, height and λ_z respectively equal to 0.5 mm, 1.25 mm and 4 mm.

The origin of the reference frame is located at the center of the rotor (Fig. 1). The x-axis is directed along the center-line of the diffuser and is positive in the streamwise direction; the y-axis is oriented in the wall-normal direction and the z-axis is such to have a left-hand oriented reference system.

The simulation domain is a box of length equal to 23 c_{diff} in the streamwise direction, and 26 c_{diff} in the $y-z$ plane. The rotor plane is placed 9 c_{diff} downstream of the inlet. Free-stream inlet boundary conditions are applied at $x = -9\,c_{diff}$ while pressure outlet boundary conditions are applied at $x = 14\,c_{diff}$. Slip boundary conditions are applied at the other walls. A total of 11 mesh refinement regions, named as VR, with resolution factor equal to 2 are employed. They are detailed in Fig. 3 only near the DAWT where regions with the same resolution are displayed with the same color. The region with the highest resolution is the offset around the zig-zag trip, where the voxel size is 4.167×10^{-1} m, corresponding to 2400 voxel per diffuser chord. This results in a distribution of $y+$ as shown in Fig. 4 for the finest resolution case investigated. In total, approximately 284 million voxels and 52 million surfels are used to discretize the problem. The flow-simulation time, for the fine case investigated, is 1.42 s (9 rotor revolutions) requiring 7200 CPU hours per revolution on a Linux Xeon E5-2690 2.9 GHz platform. In order to reduce the computational cost, each computation was seeded with the coarser one as done in previous studies [42,43].

The physical time step, corresponding to a Courant-Friedrichs-Lewy (CFL) number of 1 in the finest mesh resolution level, is 7.27×10^{-7} s. The unsteady pressure on the surface of the DonQi® wind turbine is sampled with a frequency of 10 kHz ($St_{c_{diff}} = fc_{diff}/U_\infty = 2000$) for a physical time of 1 s (equals to 6 rotor revolution).

4. Grid resolution study

Grid resolution study is carried out to verify that the solution is not dependent on the computational grid. Three grid resolutions are investigated corresponding to the smallest voxel size equal to 1200 (coarse), 1800 (medium) and 2400 (fine) voxels per diffuser chord. This is achieved by proportionally increasing the resolution of each refinement region. The corresponding number of fine equivalent voxels N for the three configurations is 1.46×10^6, 2.67×10^6 and 4.33×10^6.

The blade thrust coefficient C_t and the diffuser aerodynamic force coefficient C_F are used for the convergence analysis. They are defined as:

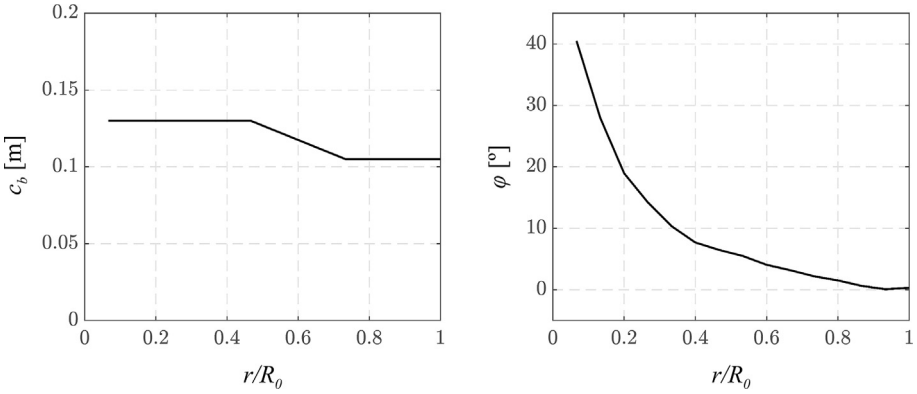

Fig. 2. Radial distribution of the rotor blade chord and twist angle.

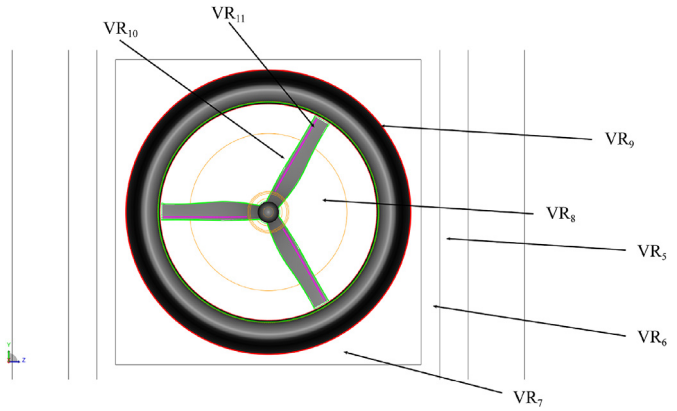

Fig. 3. Volume resolution (VR) region distribution near the DonQi® wind turbine geometry.

$$C_t = \frac{T}{\frac{1}{2}\rho U_\infty^2 A_{rot}}, \tag{7}$$

$$C_F = \frac{F}{\frac{1}{2}\rho U_\infty^2 A_{rot}}, \tag{8}$$

where T is the thrust, i.e. the axial force, generated by the wind turbine, F is the total aerodynamic force generated by the duct and A_{rot} is the rotor area equal to πR_0^2, where R_0 varies with the configuration.

Results of the convergence study are shown in Fig. 5 for both configurations. For the smaller TC configuration, the convergence study is carried out only for the medium and fine cases because of the grid dependent result found for the baseline case. Results show that convergence is reached for both hydrodynamic quantities with maximum variation between the medium and fine cases lower than 4% and 1% for the C_t and C_F, respectively. In the figure, C_F is further compared with the experimental results from ten Hoopen [44] on the same geometry showing good agreement. It is worth mentioning that in the reference publication the C_F is expressed using the exit area as reference surface, but in Fig. 5 (right) it has been expressed using the rotor area.

The figures further show that, reducing the TC from 2.5% to 0.7%, the C_t of the blades reduces of about 5%. This is due to the lower velocity at the rotor plane induced by the lift generated by the diffuser. It has been verified that a similar effect is found for the dimensional parameters; this is because the difference between the two areas is very small thus not affecting the reported observations.

The dependence of the C_t on the TC shall be considered as a guideline for the design of DAWT. As a matter of fact, DAWT are equipped with an acoustic liners like perforated surface in correspondence of the rotor plane to dampen the rotor tonal noise. This surface can alter the development of the boundary layer triggering transition or altering the boundary layer thickness at the rotor plane. This causes the reduction of thrust discussed before in addition to noise increase as will be shown in the following sections.

To complete the assessment of the computational methodology, the time-averaged pressure coefficient of the duct C_p for the baseline case with TC = 2.5% is plotted against the experimental value from ten Hoopen [44] in Fig. 6. The small discrepancies are due to the differences between the experimental setup and the computational one. The latter has noise dampeners not present in the computations.

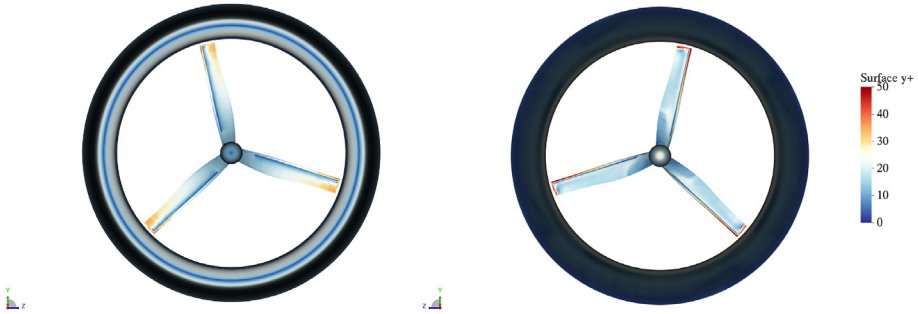

Fig. 4. Surface $y+$ distribution. (left) front and (right) back view.

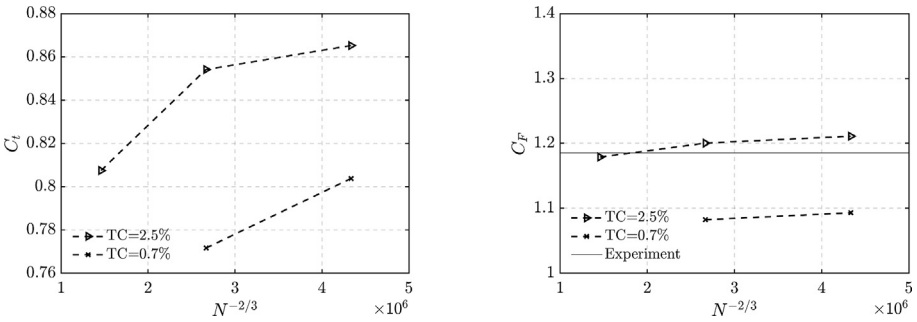

Fig. 5. (Left) Rotor thrust coefficient C_t and (right) total aerodynamic force coefficient generated by the duct C_F versus the number of equivalent fine voxels N. Experimental data taken from ten Hoopen [44].

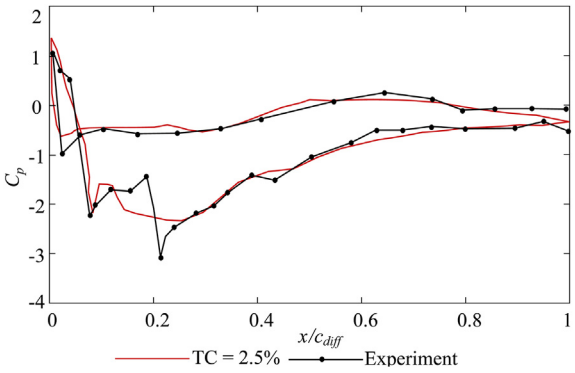

Fig. 6. Time-averaged C_p obtained from simulations compared against the experiments from ten Hoopen [44].

5. Flow field description

Visualizations of the instantaneous flow field for the baseline DonQi® DAWT (TC = 2.5%) and the one with longer blade (TC = 0.7%) show the main aerodynamic flow features (Fig. 7). In the figures, iso-surfaces of the λ_2 criterion [45] color contoured with the velocity magnitude are plotted. A zoom of the tip-gap region is also plotted in Fig. 8, where iso-surfaces of the λ_2 criterion are colored in yellow; three streamwise planes, reporting contours of the velocity magnitude and streamlines color-contoured with the velocity magnitude, are added to show the flow distortion in the near wake of the rotor.

Relevant differences are visible between the two cases. For the baseline configuration, tip vortices are generated and convected in the duct. These vortices, while convecting along a helicoidal path, become unstable and break down to turbulent flow structures (Fig. 7 left). Focusing on the vortex formation, Fig. 8 (left) shows that two vortices are generated by the passage of the rotor blade near the diffuser suction side. The inflow velocity at the rotor plane varies in the radial direction with a maximum toward the tip of the blade. Here, the flow accelerates into the gap, that acts as a convergent nozzle, injecting momentum in the boundary layer. The tip vortex is then generated above this high speed region; it induces the formation of a counter-rotating secondary vortex as visible from the λ_2 iso-surface. In the region between the two vortices, a localized low speed region is formed that becomes less intense away from the blade. The reduction of the shear forces between the tip vortex and the near wake flow reduces the strength of the secondary-induced vortex (Fig. 7 left). On the other hand, the tip vortex convects downstream and, as expected, is subject to wake expansion i.e. radial spreading toward the inner surface of the diffuser (Fig. 9). For this particular case, the curvature of the airfoil is such that no interaction with the surface of the diffuser is present. From a deeper look at the vortex instability, a spatial modulation of the convecting tip vortex is visible with the appearance of flow instabilities that induce the breakdown of the main vortex into smaller structures. The development of such instability resembles the vortex dynamics breakdown, initiated by a vortex pairing instability identified by Lignarolo et al. [46] for a conventional wind

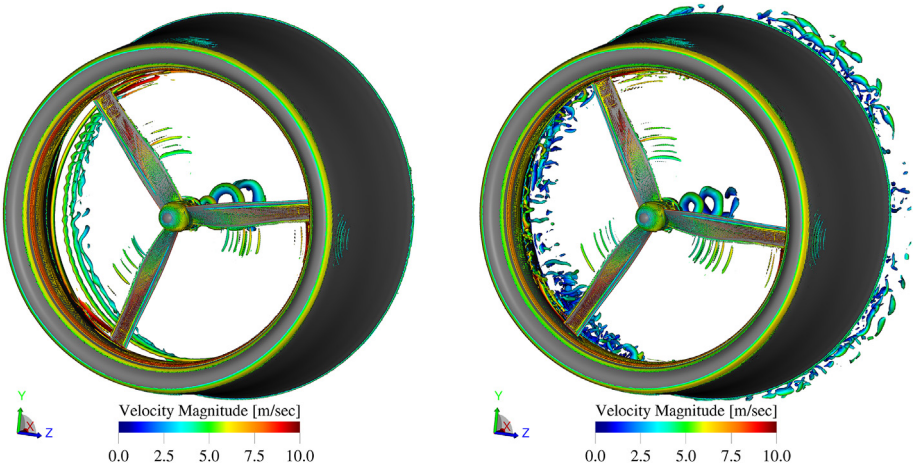

Fig. 7. Visualization of the instantaneous flow field for the DonQi® DAWT with TC = 2.5% (left) and TC = 0.7% (right). Iso-surface of the λ_2 criterion color contoured with the velocity magnitude. (For interpretation of the references to color in this figure legend, the reader is referred to the Web version of this article.)

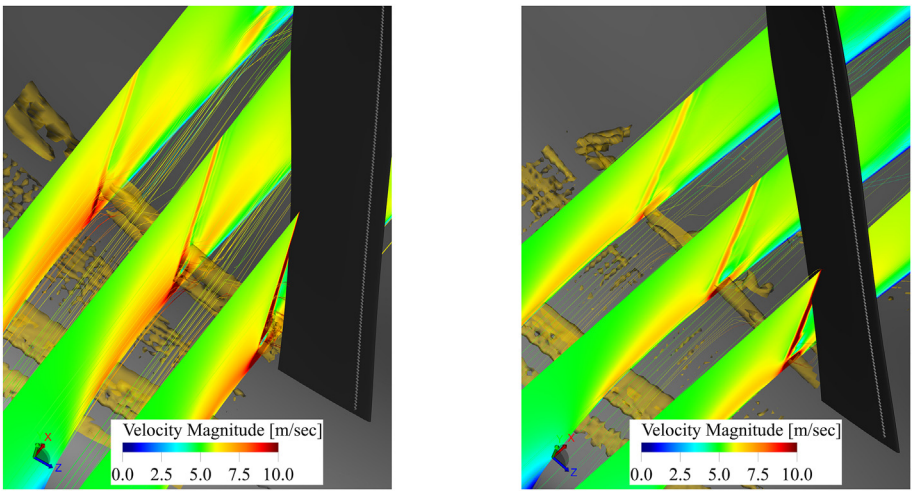

Fig. 8. Zoomed view near the blade's tip of the instantaneous flow field for the DonQi® DAWT with TC = 2.5% (left) and TC = 0.7% (right). In the figure, iso-surfaces of the λ_2 criterion are colored in yellow, three streamwise-oriented plane show contours of the velocity magnitude and the streamlines are color-contoured with the velocity magnitude. (For interpretation of the references to color in this figure legend, the reader is referred to the Web version of this article.)

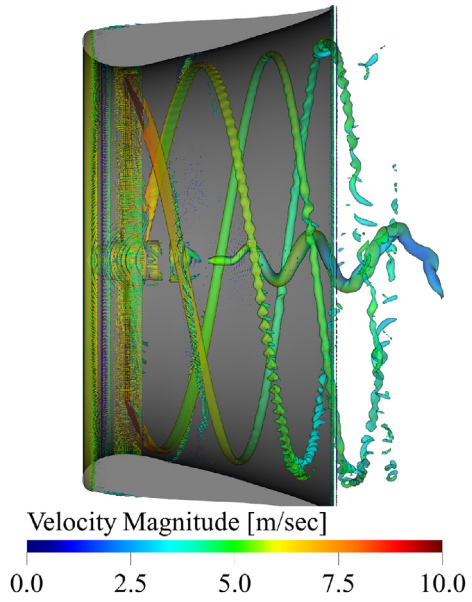

Fig. 9. Side view of the instantaneous flow field for the DonQi® DAWT with TC = 2.5% (left). Iso-surface of the λ_2 criterion color contoured with the velocity magnitude. (For interpretation of the references to color in this figure legend, the reader is referred to the Web version of this article.)

turbine.

The smaller TC configuration shows a completely different vortex dynamics (Fig. 7) with immediate breakdown of the flow structures behind the rotor plane. The acceleration of the flow in the near wake is less intense because of the rotation orientation of the tip vortex. Then, a less strong shear force and a less intense low speed region in the near wake is present, thus reducing the strength of the secondary-induced vortex that is not visible for the selected value of λ_2. As a consequence, there is reduction of momentum injected in the boundary layer with respect to the baseline case, thus promoting flow separation. For the current configuration, because of the wake expansion, the tip vortex interacts with the diffuser suction side and breaks up.

The interaction of the tip vortex with the turbulent boundary layer influences its convection over the diffuser suction side. This is visible in Fig. 12, where contours of the instantaneous streamwise velocity at the center line $x-y$ plane are plotted for the two configurations. For the baseline DAWT, the footprint of the tip vortices is visible as local high and low-speed regions. In this case, the flow is attached to the diffuser up to the 90% of the diffuser chord where separation starts. Conversely, for the smaller TC case, the tip vortex is not visible and separation starts at 70% of the diffuser chord. As discussed before, the delay of the separation for the baseline case can be attributed to the injection of momentum into the boundary layer via the vortices close to the wall.

Flow separation has a direct consequence on the lift generated by the diffuser, the velocity at the rotor plane and the thrust generated by the wind turbine. The pressure coefficient C_p distribution over the diffuser is shown in Fig. 11. The C_p curve for the smaller tip-clearance configuration is embedded into the one of the baseline case. This suggests that, for the same airfoil angle of attack, the airflow sees a thinner airfoil that generates less lift and lower mass flow rate through the duct [13]. The plateau in the C_p distribution starting from 70% of the diffuser chord agrees with the flow separation visible from the instantaneous flow organization. As a direct consequence of the C_p distribution, the flow accelerates less and the velocity at the rotor plane decreases. This is shown in Fig. 12, where the time-averaged streamwise velocity u in the axial direction at different radial locations is plotted. As expected, the inflow velocity at the rotor plane is not uniform in the radial direction with an increase up to 60% and 40% with respect to the free-stream velocity at the location of the tip for the baseline and longer blade, respectively. The difference between the two configurations is stronger toward the tip where the effect of the flow acceleration is expected to be larger. The lower velocity at the tip of the blade reduces the thrust generated by the wind turbine as shown in Fig. 13, where the cumulative sum of the thrust coefficient C_t in the radial direction is plotted. The figure confirms that minor differences are present up to $50\%R_0$ in agreement with the previous observations about the velocity at the rotor plane. Closer to the tip the effect of the velocity increase appears as local increment of thrust.

As a consequence of flow separation, the near wake flow field varies between the two configurations. This is shown in Fig. 14 where the time-averaged streamwise velocity component u is plotted in the wake at two streamwise locations $x/R_0 = 0.67$ and $x/R_0 = 1$. The figure shows that, in the near wake of the DAWT, the

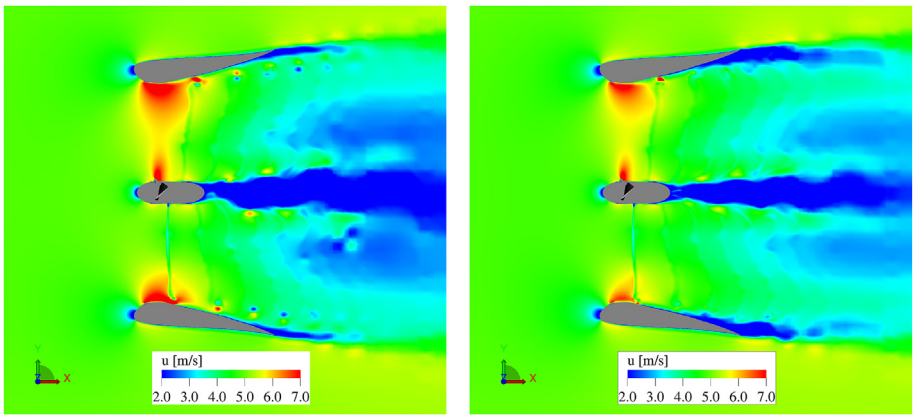

Fig. 10. Instantaneous streamwise velocity u in a center line plane for the TC = 2.5% (left) and TC = 0.7% (right).

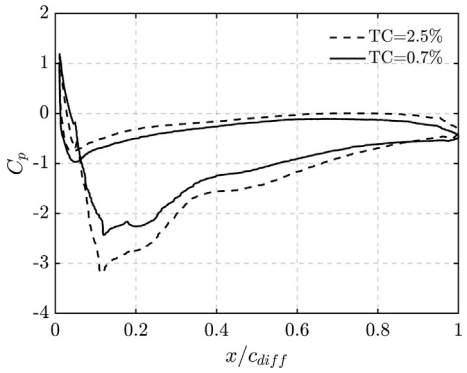

Fig. 11. Time-averaged pressure coefficient C_p along the chord of the diffuser.

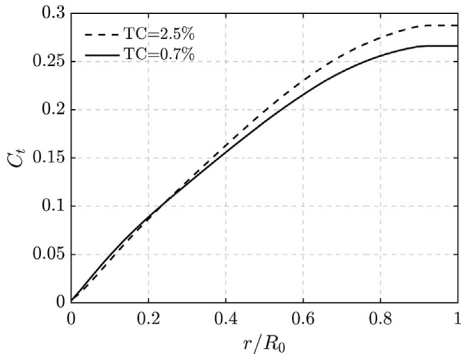

Fig. 13. Cumulative sum along the blade radius r of the thrust coefficient C_t.

configuration with the smaller TC shows a smaller wake deficit (i.e., higher velocity) as expected from the previous discussion on C_t. Independently on the streamwise location, the difference in streamwise velocity between the two configurations is almost constant and equal to $10\%U_\infty$ up to $r/R_0 = 1.2$, where the shear layer starts. Within the shear layer, the trend is opposite with the configuration with the smaller TC showing lower velocity. This can be related to the wider wake because of flow separation visualized in Fig. 10.

6. Far-field noise

The effect of the TC on the acoustic behavior of the DAWT is investigated in this section. Far-field noise is computed using the FWH acoustic analogy as discussed in section 2.2. Far-field data are obtained on a circular array of equally spaced microphones placed at $2R_0$ from the center of the duct. Two circular arrays, one in the $x-y$ plane and one in the $x-z$ plane, with 36 microphones per arc are used. The angular spacing between the microphones is 10°. In the figure, 0° corresponds to the upstream axial direction.

Fig. 15 shows the Overall Sound Pressure Level (OASPL) in a cross plane. It is expressed in dB with reference pressure equal to 20×10^{-6} Pa. Results are integrated from 2 Hz to 392.4 Hz, i.e. up to 20 times the Blade Passing Frequency (BPF). Because of the symmetric nature of the acoustic field, results from the four arcs are averaged. The figure shows that reducing the TC an increase in

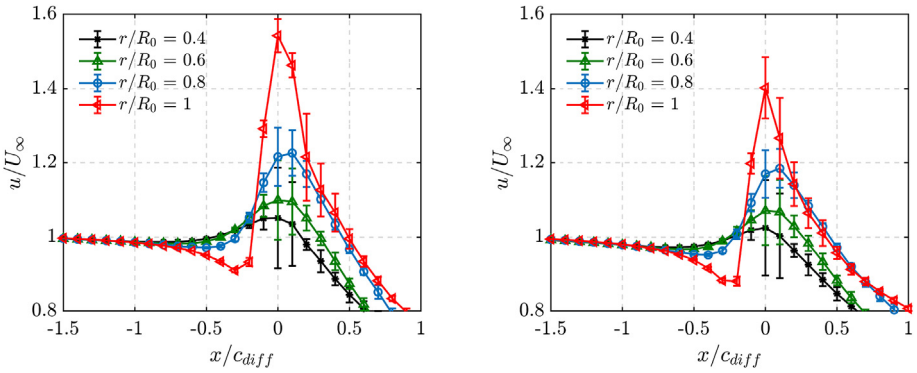

Fig. 12. Time-averaged streamwise velocity u in the axial direction at different radial locations for the TC = 2.5% (left) and TC = 0.7% (right).

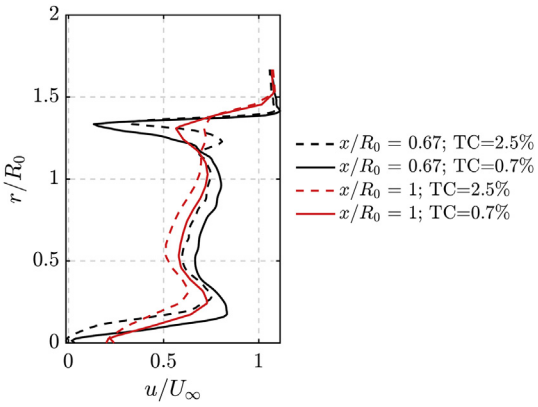

Fig. 14. Time-averaged streamwise velocity u in the wake of the ducted wind turbine for both TC at two axial locations $x/R_0 = 0.67$ and $x/R_0 = 1$

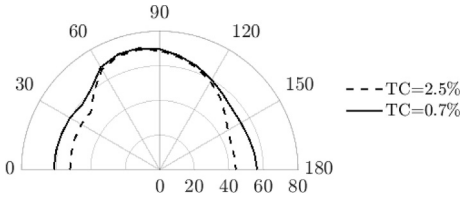

Fig. 15. Overall Sound Pressure Level (OASPL) obtained from an arc of 10 equally spaced microphones located at $2R_0$ from the center of the rotor.

noise, up to 10 dB and 5 dB respectively downstream and upstream of the DAWT, is found without a relevant variation of the directivity pattern. In the range between 60° and 120°, no variation between the two cases is found. In this range, the directivity pattern is oriented upstream with a relative maximum at 70°. Both directivity patterns are different from the one of an isolated wind turbine where a shadow region is expected at about 90°. This can be due to the presence of the duct that acts as a shielding surface for noise sources within it, thus altering the direction of noise propagation.

To better describe the acoustic field, Sound Power Level (PWL) versus the BPF is reported in Fig. 16. PWL is obtained integrating the data from the spherical distribution of microphones and it is expressed in dB. It shows that the tonal noise due to the rotor loading is the dominant source of noise. The decaying broadband part of the spectrum is instead associated to turbulent-boundary-layer trailing-edge noise at the trailing edge of both the duct and the rotor blades [47]. For both configurations the first two BPFs

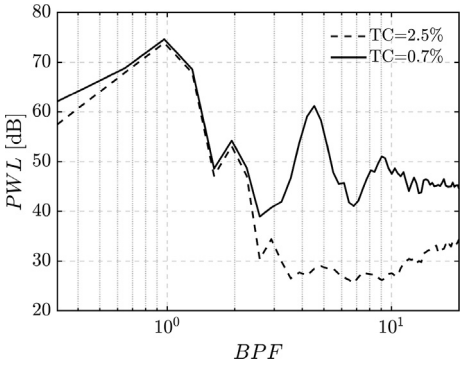

Fig. 16. Sound Power Level (PWL) versus the Blade Passing Frequency (BPF) obtained from integration from the four arcs of microphones located at $2R_0$ from the center of the rotor.

have the same power intensity. The power associated with the first BPF is approximately 20 dB larger then the second. At frequencies higher than the second BPF the two curves diverge; the configuration with smaller TC shows larger broadband noise with amplitude larger than the tonal peak corresponding to the third BPF of the larger TC case. The increase of the broadband component at higher frequency can be caused by the larger intensity of the turbulent fluctuations due to flow separation. A similar trend has been recently discovered for small propellers and was attributed to unsteady flow [48]; in this case, it might be caused by the interaction between the tip of the blade and turbulent boundary layer as it will be discussed later. For the small TC configuration, additional tonal peaks arise at frequency equal to 4.5 BPF and its harmonics that cannot be associated to the rotor noise. The physical nature of this source of noise can be linked to an increase of the turbulent velocity fluctuations as observed for fan noise by Fukano and Jang [16]. They found that noise increases by decreasing the mass flow rate, by increasing the TC and that it is relevant for frequencies lower than the fourth BPF. Conversely, for the DAWT, it is found that this source of noise dominates at frequencies higher than the fourth BPF and that it appears when reducing the TC. The opposite trend for DAWT can be due to the different working principles of the two systems.

The physical mechanisms behind this source of noise are further investigated by plotting the Power Spectral Density (PSD) versus the BPF, expressed in dB/Hz, for three microphones located at 30°, 90° and 120° and radial distance equal to $2R_0$ in Fig. 17. It confirms that the tone associated with the second noise source is dominant in the upstream and downstream directions where its intensity is comparable or higher than the ones of the first two BPFs. More interesting, the energy associated with this source of noise is similar for the three directions, suggesting that it might be modeled as a monopole source of sound in the gap. This observation can explain the OSPL directivity plot in Fig. 15: the variation of TC causes similar noise directivity plot with noise increase of similar intensity both upstream and downstream of the DAWT; the same OSPL intensity between the two configurations in the radial direction is instead associated to the presence of the duct that acts as a shielding surface for a source located within it.

The previous observations are further supported by the band-pass filtered time derivative of the pressure field in Fig. 18. The figures correspond to central frequency equal to the first BPF (top) and 4.5 times the BPF (bottom). The baseline case is represented on the left while the shorter tip clearance configuration on the right. The fist row confirms that for both cases noise is generated by the rotor. Conversely, the second row shows that for the shorter tip clearance, an additional source of noise can be localized in the tip gap region with intensity comparable to the one of the first BPF. This source of noise is mainly oriented in the axial location and weakly affect noise between 60° and 90° as discussed before. Despite the presence of large vortical structures in the wake, no additional noise source is detected.

As stated before, for fan applications, this source of noise is associated to an increase of the velocity fluctuations in the tip gap region. The effect of the amplification of the velocity fluctuations is shown in Fig. 19. Here the band-pass filtered streamwise velocity component for central frequency equal to 4.5 times the BPF is displayed. The baseline case is represented on the left while the shorter tip clearance configuration on the right. The figure shows a different pattern of the turbulent flow structures near the blade. Comparing the two configurations, it is evident that, for the shorter tip clearance configuration, the near wake of the tip show higher energy content in this frequency band while both configurations show a similar spatial distribution of the velocity fluctuations.

To better assess that the increase of the velocity fluctuations is the main physical mechanism associated to the noise increase at

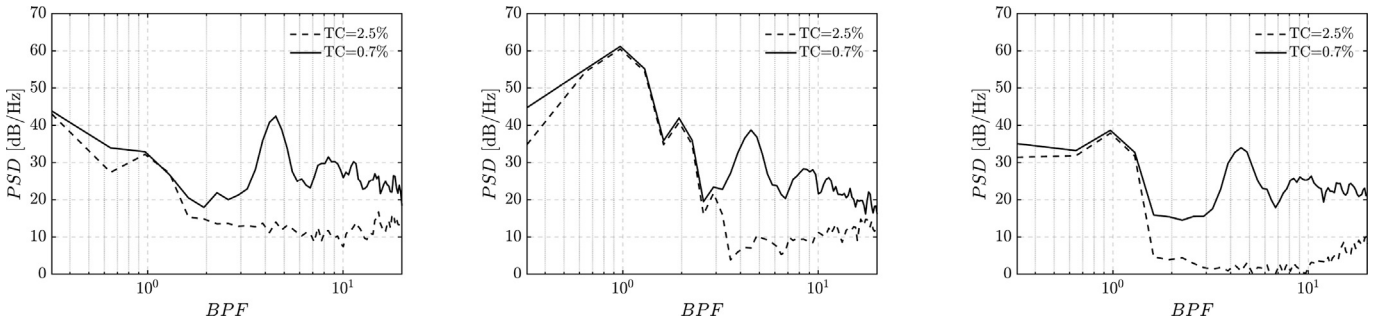

Fig. 17. Power Spectral Density (PSD) versus the Blade Passing Frequency (BPF), for three microphones located at 30°, 90° and 120° and radial distance equal to $2R_0$.

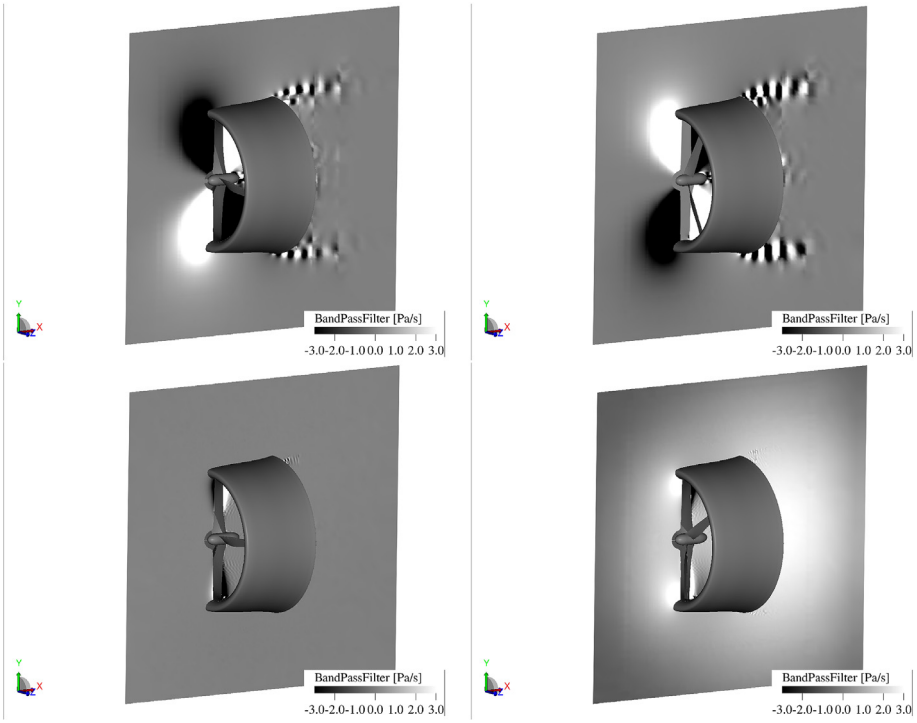

Fig. 18. Band-pass filtered time derivative of the pressure field for central frequency corresponding to the first blade passing frequency (top) and 4.5 times the blade passing frequency (bottom). The TC = 2.5% case is displayed on the left while the TC = 0.7% case on the right.

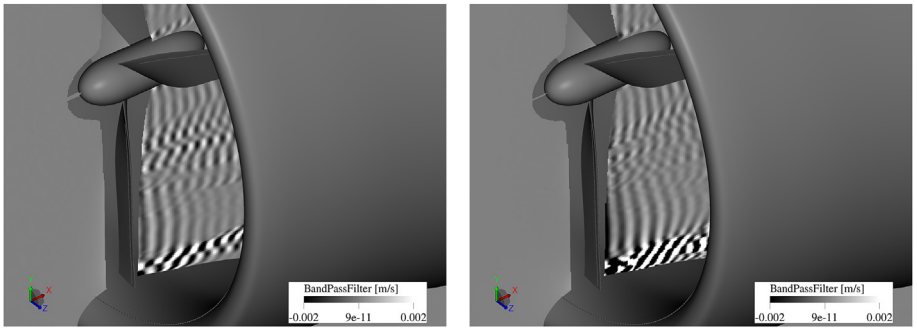

Fig. 19. Band-pass filtered time derivative of the streamwise velocity component for central frequency equal to 4.5 times the blade passing frequency. The TC = 2.5% case is displayed on the left while the TC = 0.7% case on the right.

frequencies higher than the third BPF, the spectra of the streamwise velocity component Φ_{uu} are plotted in Fig. 20. Here spectra at two locations, upstream ($x/R_0 = -0.13$, $y/R_0 = 1.0$) and downstream ($x/R_0 = 0.13$, $y/R_0 = 1.04$) of the blades are plotted. The figure shows that the turbulent fluctuations increase behind the blade and that, for the shorter TC case, an increase with respect to the baseline case, is present at frequency higher than the third BPF in agreement with the acoustic results (Figs. 16 and 17). An additional

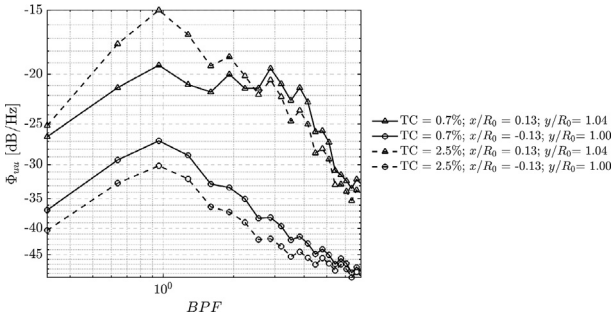

Fig. 20. Spectra of the streamwise velocity component Φ_{uu} at two point in front and behind the tip gap region.

small peak is measured at a frequency equal to 4.5 times the BPF which can be linked to the observed tonal noise at this frequency.

7. Conclusions

The effect of the tip-clearance ratio for a DAWT on both the flow field and the far-field noise is investigated with LB-VLES. Two DAWT configurations are investigated. They differ for the tip-clearance ratio, defined as the ratio between the tip clearance and the rotor radius. The DonQi® wind turbine, a three blade ducted rotor, is adopted as reference configuration. It has a tip clearance ratio of 2.5%. The second configuration is obtained from the first one by elongating the rotor radius such to force the interaction between the turbulent boundary layer developing over the suction side of the diffuser and the tip of the blades, thus resulting in a tip-clearance ratio of 0.7%.

Comparing the two configurations, it is found that the rotor with the longer blades shows a reduction of the rotor thrust coefficient because of the lower lift generated by the diffuser that results in a lower axial velocity at the rotor plane up to 13% with respect to the baseline case. Three-dimensional flow visualizations through the λ_2 criterion and contour of the instantaneous streamwise velocity component show that this is caused by the smaller tip gap that forces the break down of the rotor tip vortex in smaller turbulent structures immediately after the rotor plane and that induces earlier flow separation along the suction side of the diffuser. Conversely, for the shorter blade configuration, the tip vortex convects almost undisturbed in the duct following a helicoidal path and transition to turbulence. The distribution of the pressure coefficient along the duct surface, for the longer blades, is embedded within the one with larger tip clearance showing that, because of the interaction, a thinner airfoil is seen by the incoming flow. For the longer blade, a local maximum in the surface pressure is found in correspondence of the leading edge of the tip section due to the flow deceleration induced by the interaction.

The tip clearance ratio has also a strong effect on the far-field noise showing up to 10 dB increase in the axial direction downstream of the rotor. For angles between 60° and 120°, where 0° corresponds to the axial upstream direction, the blade tonal noise, at frequencies equal to the blade passing frequency and higher harmonics, is the dominant source. For other angular directions, noise increase is found for the smaller tip-clearance ratio case. This is associated to an additional noise source due to an increase of the energy content of velocity fluctuations in the gap region. This noise source has the same intensity in all the directions and can be modeled as a monopole source located in the gap. It causes an increase of broadband noise at frequencies higher than the third blade passing frequency and tonal peaks at frequencies equal to 4.5 times the blade passing frequency and higher harmonics.

Declaration of competing interest

The authors declare that they have no known competing financial interests or personal relationships that could have appeared to influence the work reported in this paper.

CRediT authorship contribution statement

Francesco Avallone: Data analysis, Writing - review and editing. **Daniele Ragni:** Writing - review and editing. **Damiano Casalino:** Writing - review and editing.

Acknowledgement

The authors would like to acknowledge the DUCT4U project (NWO grant number 12728) for providing the reference geometry.

References

[1] I. Pineda, P. Tardieu, Wind in Power 2016 European Statistics, Tech. Rep., Wind Europe, 2017 https://windeurope.org/wp-content/uploads/files/about-wind/statistics/WindEurope-Annual-Statistics-2016.pdf.
[2] P. Tardieu, Wind Energy in Europe: Scenarios for 2030, Tech. Rep., 2017 https://windeurope.org/wp-content/uploads/files/about-wind/reports/Wind-energy-in-Europe-Scenarios-for-2030.pdf.
[3] C. Shonhiwa, G. Makaka, Concentrator augmented wind turbines: a review, Renew. Sustain. Energy Rev. 59 (2016) 1415–1418, https://doi.org/10.1016/J.RSER.2016.01.067. https://www.sciencedirect.com/science/article/pii/S1364032116000976.
[4] A. Agha, H. Chaudhry, F. Wang, Diffuser augmented wind turbine (DAWT) technologies: a review, Int. J. Renew. Energy Resour. 8 (3) (2018) 1369–1385. http://mail.ijrer.org/ijrer/index.php/ijrer/article/view/7794.
[5] A. von Betz, Energieumsetzungen in venturidusen, Die Naturiwissenschaften 10 (1929) 160–164.
[6] R. Bontempo, M. Manna, Solution of the flow over a non-uniform heavily loaded ducted actuator disk, J. Fluid Mech. 728 (2013) 163–195, https://doi.org/10.1017/jfm.2013.257. https://www.cambridge.org/core/services/aop-cambridge-core/content/view/S0022112013002577.
[7] O. de Vries, Fluid dynamic aspects of wind energy conversion, Tech. Rep. (1979). AGARD-AG-243.
[8] M. Hansen, N. Sørensen, R. Flay, Effect of placing a diffuser around a wind turbine, Wind Energy 3 (4) (2000) 207–213, https://doi.org/10.1002/we.37, 10.1002/we.37.
[9] G. van Bussel, The science of making more torque from wind: diffuser experiments and theory revisited, J. Phys. Conf. 75 (1) (2007), https://doi.org/10.1088/1742-6596/75/1/012010, 012010, http://stacks.iop.org/1742-6596/75/i=1/a=012010?key=crossref.7ffed872e5c605cfed31a3f49ba9c897.
[10] P. Jamieson, Generalized limits for energy extraction in a linear constant velocity flow field, Wind Energy 11 (5) (2008) 445–457, https://doi.org/10.1002/we.268, 10.1002/we.268.
[11] M. Werle, W. Presz, Ducted wind/water turbines and propellers revisited, J. Propul. Power 24 (5) (2008) 1146–1150, https://doi.org/10.2514/1.37134. http://arc.aiaa.org/doi/10.2514/1.37134.
[12] T. Khamlaj, M. Rumpfkeil, Theoretical analysis of shrouded horizontal Axis wind turbines, Energies 10 (12) (2017) 38, https://doi.org/10.3390/en10010038. http://www.mdpi.com/1996-1073/10/1/38.
[13] G. De Oliveira, R. Pereira, D. Ragni, F. Avallone, G. Van Bussel, How does the presence of a body affect the performance of an actuator disk ?, J. Phys. Conf. 753 (2), ISSN 17426596, doi:10.1088/1742-6596/753/2/022005.
[14] V. Dighe, G. de Oliveira, F. Avallone, G. van Bussel, Towards improving the aerodynamic performance of a ducted wind turbine: a numerical study, J. Phys. Conf. 1037 (2) (2018), https://doi.org/10.1088/1742-6596/1037/2/022016, 022016, http://stacks.iop.org/1742-6596/1037/i=2/a=022016?key=crossref.60e6e81cfa484a66a59fed1611d04f64.
[15] V. Dighe, F. Avallone, G. van Bussel, Computational study of diffuser augmented wind turbine using actuator disc force method, International Journal of Computational Methods and Experimental Measurements 4 (4) (2016) 522–531, https://doi.org/10.2495/CMEM-V4-N4-522-531. http://www.witpress.com/journals/CMEM-522-531.
[16] T. Fukano, C.-M. Jang, Tip clearance noise of axial flow fans operating at design and off-design condition, J. Sound Vib. 275 (3–5) (2004) 1027–1050, https://doi.org/10.1016/S0022-460X(03)00815-0. https://www.sciencedirect.com/science/article/pii/S0022460X03008150.
[17] K. Abe, Y. Ohya, An investigation of flow fields around flanged diffusers using CFD, J. Wind Eng. Ind. Aerod. 92 (3–4) (2004) 315–330, https://doi.org/10.1016/J.JWEIA.2003.12.003. https://www.sciencedirect.com/science/article/pii/S0167610503002113.
[18] Y. Ohya, T. Uchida, T. Karasudani, M. Hasegawa, H. Kume, Numerical studies of flow around a wind turbine equipped with a flanged-diffuser shroud using an

actuator-disk model, Wind Eng. 36 (4) (2012) 455–472, https://doi.org/10.1260/0309-524X.36.4.455. http://journals.sagepub.com/doi/10.1260/0309-524X.36.4.455.
[19] M. Kardous, R. Chaker, F. Aloui, S. Nasrallah, On the dependence of an empty flanged diffuser performance on flange height: numerical simulations and PIV visualizations, Renew. Energy 56 (2013) 123–128, https://doi.org/10.1016/J.RENENE.2012.09.061. https://www.sciencedirect.com/science/article/pii/S0960148112006611.
[20] S. Hjort, H. Larsen, A multi-element diffuser augmented wind turbine, Energies 7 (5) (2014) 3256–3281, https://doi.org/10.3390/en7053256. http://www.mdpi.com/1996-1073/7/5/3256.
[21] A. Aranake, K. Duraisamy, Aerodynamic optimization of shrouded wind turbines, Wind Energy 20 (5) (2017) 877–889, https://doi.org/10.1002/we.2068, 10.1002/we.2068.
[22] N. Bagheri-Sadeghi, B. Helenbrook, K. Visser, Ducted wind turbine optimization and sensitivity to rotor position, Wind Energy Science 3 (1) (2018) 221–229, https://doi.org/10.5194/wes-3-221-2018. https://www.wind-energ-sci.net/3/221/2018/.
[23] Ffwocs Williams J., Hawkings D., Sound generation by turbulence and surfaces in arbitrary motion, Phil. Trans. Roy. Soc. Lond.: Mathematical, Physical and Engineering Sciences 264 (1151) (n.d.), doi:10.1098/rsta.1969.0031.
[24] M. Khorrami, E. Fares, D. Casalino, Towards full aircraft airframe noise prediction: lattice Boltzmann simulations, in: 20th AIAA/CEAS Aeroacoustics Conference, American Institute of Aeronautics and Astronautics, Atlanta, Georgia, 2014, ISBN 978-1-62410-285-1, https://doi.org/10.2514/6.2014-2481. AIAA 2014–2481, http://arc.aiaa.org/doi/10.2514/6.2014-2481.
[25] D. Casalino, A. Hazir, A. Mann, Turbofan broadband noise prediction using the lattice Boltzmann method, AIAA J. (2017) 1–20, https://doi.org/10.2514/1.J055674. https://arc.aiaa.org/doi/10.2514/1.J055674.
[26] Avallone F., Van Der Velden W., Ragni D., Casalino D., Noise reduction mechanisms of sawtooth and combed-sawtooth trailing-edge serrations, J. Fluid Mech. 848, ISSN 14697645 (n.d.), doi:10.1017/jfm.2018.377.
[27] S. Succi, The Lattice Boltzmann Equation for Fluid Dynamics and Beyond, first ed., Clarendon Press, Oxford, 2001.
[28] X. Shan, X.-F. Yuan, H. Chen, Kinetic theory representation of hydrodynamics: a way beyond the Navier–Stokes equation, J. Fluid Mech. 550 (2006) 413–441, https://doi.org/10.1017/S0022112005008153. http://www.journals.cambridge.org/abstract_S0022112005008153.
[29] S. Chen, G. Doolen, Lattice Boltzmann method for fluid flows, Annu. Rev. Fluid Mech. 30 (1) (1998) 329–364, https://doi.org/10.1146/annurev.fluid.30.1.329. ISSN 0066-4189, http://www.annualreviews.org/doi/10.1146/annurev.fluid.30.1.329.
[30] H. Chen, S. Chen, W. Matthaeus, Recovery of the Navier-Stokes equations using a lattice-gas Boltzmann method, Phys. Rev. 45 (8) (1992) R5339–R5342, https://doi.org/10.1103/PhysRevA.45.R5339. https://link.aps.org/doi/10.1103/PhysRevA.45.R5339.
[31] H. Chen, R. Zhang, P. Gopalakrishnan, Lattice Boltzmann Collision Operators Enforcing Isotropy and Galilean Invariance, 2015. https://patents.google.com/patent/US20150356217A1/en.
[32] V. Yakhot, S. Orszag, Renormalization group analysis of turbulence. I. Basic theory, J. Sci. Comput. 1 (1) (1986) 3–51, https://doi.org/10.1007/BF01061452. http://link.springer.com/10.1007/BF01061452.
[33] C. Teixeira, Incorporating turbulence models into the lattice-Boltzmann method, Int. J. Mod. Phys. C (1998) 1159–1175, https://doi.org/10.1142/S0129183198001060, 09 (08), http://www.worldscientific.com/doi/abs/10.1142/S0129183198001060.
[34] D. Wilcox, Turbulence Modelling for CFD, third ed., DCW Industries, Incorporated, 2006.
[35] B. Launder, D. Spalding, The numerical computation of turbulent flows, Comput. Methods Appl. Mech. Eng. 3 (2) (1974) 269–289, https://doi.org/10.1016/0045-7825(74)90029-2. http://www.sciencedirect.com/science/article/pii/0045782574900292.
[36] F. Farassat, G. Succi, A review of propeller discrete frequency noise prediction technology with emphasis on two current methods for time domain calculations, J. Sound Vib. 71 (3) (1980) 399–419, https://doi.org/10.1016/0022-460X(80)90422-8. ISSN 0022460X.
[37] G. Brès, F. Pérot, D. Freed, A ffowcs williams - Hawkings solver for lattice-Boltzmann based computational aeroacoustics, in: 16th AIAA/CEAS Aeroacoustics Conference, American Institute of Aeronautics and Astronautics, Stockholm, Sweden, 2010, ISBN 978-1-60086-955-6, https://doi.org/10.2514/6.2010-3711. AIAA 2010–3711, http://arc.aiaa.org/doi/10.2514/6.2010-3711.
[38] A. Najafi-Yazdi, G. Bres, L. Mongeau, An acoustic analogy formulation for moving sources in uniformly moving media, Proc. Math. Phys. Eng. Sci. 467 (2125) (2010) 144–165, https://doi.org/10.1098/rspa.2010.0172. http://rspa.royalsocietypublishing.org/cgi/doi/10.1098/rspa.2010.0172.
[39] D. Casalino, An advanced time approach for acoustic analogy predictions, J. Sound Vib. 261 (4) (2003) 583–612, https://doi.org/10.1016/S0022-460X(02)00986-0. ISSN 0022460X.
[40] N. Curle, The influence of solid boundaries upon aerodynamic sound, Proc. Roy. Soc. Lond.: Mathematical, Physical and Engineering Sciences 231 (1187) (1955) 505–514.
[41] F. van Dorst, An Improved Design for a Diffuser Augmented Wind Turbine, Ph.D. thesis, Delft University of Technology, 2011.
[42] F. Avallone, D. Casalino, D. Ragni, Impingement of a propeller-slipstream on a leading edge with a flow-permeable insert: a computational aeroacoustic study, Int. J. Aeroacoustics 17 (6–8) (2018b) 687–711, https://doi.org/10.1177/1475472X18788961. http://journals.sagepub.com/doi/10.1177/1475472X18788961.
[43] D. Casalino, F. Avallone, I. Gonzalez-Martino, D. Ragni, Aeroacoustic study of a wavy stator leading edge in a realistic fan/OGV stage, J. Sound Vib. 442 (2019) 138–154, https://doi.org/10.1016/J.JSV.2018.10.057. https://www.sciencedirect.com/science/article/pii/S0022460X18307375.
[44] P. ten Hoopen, An Experimental and Computational Investigation of a Diffuser Augmented Wind Turbine with an Application of Vortex Generators on the Diffuser Trailing Edge, Ph.D. thesis, Delft University of Technology, 2009, https://repository.tudelft.nl/islandora/object/uuid%3Af874600f-7cf3-468e-b6e7-fdadc3441077.
[45] J. Jeong, F. Hussain, On the identification of a vortex, J. Fluid Mech. 285 (1995) 69, https://doi.org/10.1017/S0022112095000462. http://www.journals.cambridge.org/abstract_S0022112095000462.
[46] L. Lignarolo, D. Ragni, F. Scarano, C. Simao Ferreira, G. van Bussel, Tip-vortex instability and turbulent mixing in wind-turbine wakes, J. Fluid Mech. 781 (2015) 467–493, https://doi.org/10.1017/jfm.2015.470. http://www.journals.cambridge.org/abstract_S002211201500470X.
[47] T. Brooks, D. Pope, M. Marcolini, Airfoil Self-Noise and Prediction, Tech. Rep., 1989 https://info.aiaa.org/tac/ASG/FDTC/DG/BECAN_files_/BANCII_category1/documentation/Related_Papers/BPM-NASA-RP-1218-1989.pdf.
[48] C. Nardari, D. Casalino, F. Polidoro, V. Coralic, P.-T. Lew, J. Brodie, Numerical and experimental investigation of flow confinement effects on UAV rotor noise, in: 25th AIAA/CEAS Aeroacoustics Conference, American Institute of Aeronautics and Astronautics, Reston, Virginia, 2019, ISBN 978-1-62410-588-3, https://doi.org/10.2514/6.2019-2497. https://arc.aiaa.org/doi/10.2514/6.2019-2497.